Light: Science & Applications (2017) 6, e17046; doi:10.1038/lsa.2017.46
Official journal of the CIOMP 2047-7538/17
www.nature.com/lsa

ORIGINAL ARTICLE

Air quality monitoring using mobile microscopy and machine learning

Yi-Chen Wu[1,2,3], Ashutosh Shiledar[1], Yi-Cheng Li[1], Jeffrey Wong[4], Steve Feng[1,2,3], Xuan Chen[1], Christine Chen[1], Kevin Jin[1], Saba Janamian[1], Zhe Yang[1], Zachary Scott Ballard[1,2,3], Zoltán Göröcs[1,2,3], Alborz Feizi[1,2,3] and Aydogan Ozcan[1,2,3,5]

Rapid, accurate and high-throughput sizing and quantification of particulate matter (PM) in air is crucial for monitoring and improving air quality. In fact, particles in air with a diameter of $\leq 2.5\,\mu m$ have been classified as carcinogenic by the World Health Organization. Here we present a field-portable cost-effective platform for high-throughput quantification of particulate matter using computational lens-free microscopy and machine-learning. This platform, termed c-Air, is also integrated with a smartphone application for device control and display of results. This mobile device rapidly screens 6.5 L of air in 30 s and generates microscopic images of the aerosols in air. It provides statistics of the particle size and density distribution with a sizing accuracy of ~93%. We tested this mobile platform by measuring the air quality at different indoor and outdoor environments and measurement times, and compared our results to those of an Environmental Protection Agency–approved device based on beta-attenuation monitoring, which showed strong correlation to c-Air measurements. Furthermore, we used c-Air to map the air quality around Los Angeles International Airport (LAX) over 24 h to confirm that the impact of LAX on increased PM concentration was present even at >7 km away from the airport, especially along the direction of landing flights. With its machine-learning-based computational microscopy interface, c-Air can be adaptively tailored to detect specific particles in air, for example, various types of pollen and mold and provide a cost-effective mobile solution for highly accurate and distributed sensing of air quality.

Light: Science & Applications (2017) **6,** e17046; doi:10.1038/lsa.2017.46; published online 8 September 2017

Keywords: air-quality monitoring; holography; machine learning; particulate matter

INTRODUCTION

Air quality is an increasing concern in the industrialized world. According to the World Health Organization (WHO), air pollution causes two million deaths annually in China, India and Pakistan. Moreover, 'premature death' of seven million people worldwide each year is due to the health hazards of air pollution[1]. Recently, several severe incidents of pollution haze afflicted Beijing, China and attracted worldwide attention[2–4].

Particulate matter (PM) is a mixture of solid and liquid particles in air and forms a significant form of air pollution. PM sources include, for example, direct emission from a source, such as a construction site, smokestack, or fire, or a result of complex chemical reactions emitted from power plants, industrial production and automobiles[5]. PM with a general diameter of 10 μm and smaller, which is termed PM10, can cause serious health problems because it can become lodged deep in the lungs and even enter the bloodstream. A smaller PM size category, PM2.5, which represents particles with a diameter of 2.5 μm or smaller, has been declared a cause of cancer by the WHO[6]. Furthermore, PM is a major environmental issue on account of reduced visibility (haze). Monitoring PM air quality as a function of space and time is critical for understanding the effects of industrial activities, studying atmospheric models and providing regulatory and advisory guidelines for transportation, residents and industries.

Currently, PM monitoring is performed at designated air sampling stations, which are regulated by the US Environmental Protection Agency (EPA) and similar agencies in different countries. Many of these advanced automatic platforms use either beta-attenuation monitoring (BAM)[7] or a tapered element oscillating microbalance (TEOM)[7] instrument. BAM instruments sample aerosols on a rotating filter. Using a beta-particle source, they measure the beta-particle attenuation induced by the accumulated aerosols on the filter. TEOM-based instruments, on the other hand, capture aerosols in a filter cartridge, which contains a glass tube tip that vibrates at varying frequencies according to the mass of the captured aerosols. These devices provide accurate PM measurements at high throughputs. However, they are cumbersome and heavy (~30 kg), relatively expensive (approximately $50 000–100 000) and require specialized personnel or technicians for regular system maintenance, for example,

[1]Electrical Engineering Department, University of California, Los Angeles, CA 90095, USA; [2]Bioengineering Department, University of California, Los Angeles, CA 90095, USA; [3]California NanoSystems Institute (CNSI), University of California, Los Angeles, CA 90095, USA; [4]Computer Science Department, University of California, Los Angeles, CA 90095, USA and [5]David Geffen School of Medicine, University of California, Los Angeles, CA 90095, USA
Correspondence: A Ozcan, Email: ozcan@ucla.edu, Web: http://innovate.ee.ucla.edu/
Received 11 December 2016; revised 10 March 2017; accepted 11 March 2017; accepted article preview online 15 March 2017

every few weeks. Owing to these limitations, only ~ 10 000 of these air sampling stations exist worldwide.

In addition to these high-end PM measurement instruments, several commercially available portable particle counters are available at a lower cost of approximately $2000 (Refs. 8,9) and in some cases much higher, approximately $7000–8000 (Ref. 10). These commercially available optical particle counters resemble a flow-cytometer. They drive the sampled air through a small channel. A laser beam focused on the nozzle of this channel is scattered by each particle that passes through the channel. The scattering intensity is then used to infer the particle size. Because of its serial read-out nature, the sampling rate of this approach is limited to $<2–3\ \mathrm{L \cdot min^{-1}}$ and in some sub-micron particle detection schemes $<0.8\ \mathrm{L \cdot min^{-1}}$ [10]. Furthermore, accurate measurement of either very-high or very-low concentrations of particles is challenging for these devices, which limits the dynamic range of the PM measurement. In addition to these limitations, the scattering cross-section, which comprises the quantity actually measured by this device type, heavily depends on the three-dimensional (3D) morphology and refractive properties of the particles. This can cause severe errors in the conversion of the measured scattered light intensities into actual particle sizes. Finally, none of these designs offers a direct measure, that is, a microscopic image of the captured particles, which is another limitation because further analysis of a target particle of interest after its detection cannot be performed.

On account of these limitations, many air sampling activities continue to use microscopic inspection and counting. Basically, air samples are manually obtained in the field using a portable sampler that employs various processes, such as cyclonic collection, impingement, impaction, thermophoresis or filtering[11–14]. The sample is then sent to a central laboratory, where it is post-processed and manually inspected under a microscope by an expert. This type of microscopic analysis provides the major advantage of more accurate particle sizing, while enabling the expert reader to recognize the particle shape and

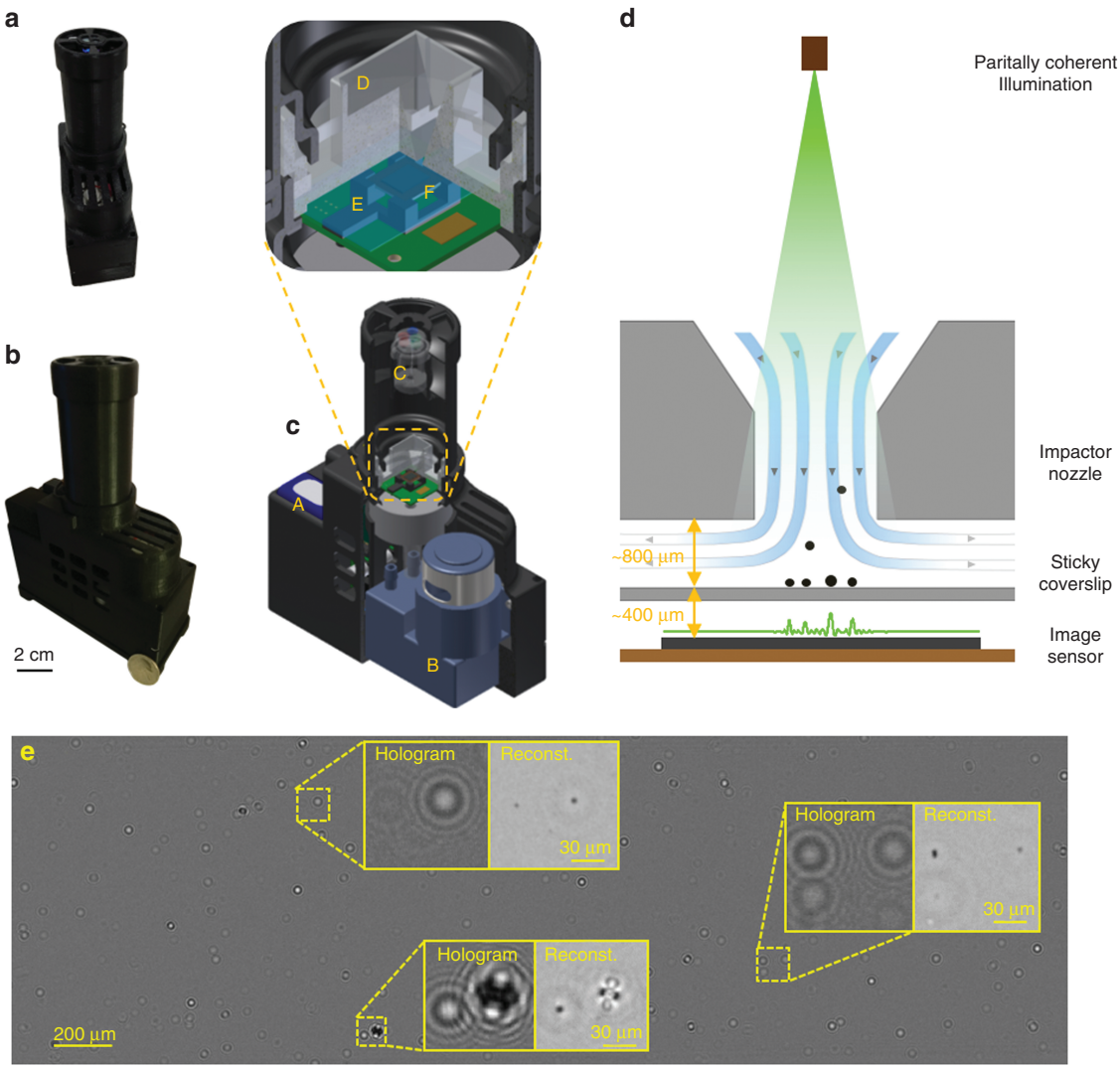

Figure 1 c-Air platform. (**a** and **b**) Photos of the device from different perspectives. A quarter is placed beside the device in **b** for scale. (**c**) 3D computer-aided-design (CAD)-drawing overview of the device, including (A) rechargeable battery, (B) vacuum pump ($13\ \mathrm{L \cdot min^{-1}}$), (C) illumination module with fiber-coupled light-emitting diodes of red (624 nm), green (527 nm) and blue (470 nm) and (D) impaction-based air sampler with (E) a sticky coverslip on top of (F) the image sensor. (**d**) Schematic drawing of impaction-based air sampler on a chip. (**e**) Whole field-of-view differential hologram image of an aerosol sample during sampling, and zoomed-in regions of its reconstruction. The device is powered by a rechargeable battery (A), and controlled by a microcontroller (Raspberry Pi A+). The assembly and packaging are 3D-printed.

doi:10.1038/lsa.2017.46

type. These capabilities yield additional benefits in more complicated analyses of air pollution, such as identification of a specific aerosol type. In this method, however, the sampling and inspection processes are separated; that is, the sampling is performed in the field, whereas the sample analysis is conducted in a remote professional lab. This significantly delays the reporting of the results. Furthermore, the inspection is manually performed by a trained expert, which considerably increases the overall cost of each air-quality measurement. Furthermore, this conventional microscope-based screening of aerosols cannot be conducted in the field, because these benchtop microscopes are cumbersome, heavy, expensive and require specialized skills to operate.

In this paper, as a transformative solution to the above outlined limitations of existing air quality measurement techniques, we present a hand-held and cost-effective platform for automated sizing and high-throughput quantification of PM using computational lens-free microscopy and machine learning. As an alternative to conventional lens-based microscopy techniques, in a computational lens-free microscopy approach, the sample is directly positioned on top of an image sensor chip with no optical components between them[15,16]. Such an on-chip microscope can rapidly reconstruct images of transmissive samples over a very large field of view of $>20\,\mathrm{mm}^2$. On the basis of this computational on-chip imaging concept and a unique machine learning enabled particle analysis method, we demonstrate in this paper the design of a lightweight (~590 g), hand-held and cost-effective air-quality monitoring system, termed c-Air. This mobile system utilizes a micro-pump, an impaction-based air-sampler and a lens-free holographic on-chip microscope that is integrated with a custom-written machine learning algorithm for remote data processing and particle analysis. The c-Air platform (Figures 1 and 2) operates with a smartphone application (app) for device control and data display. It can rapidly screen 6.5 L of air volume in 30 s, generating microscopic phase and amplitude images of the captured particles, while also automatically providing the PM

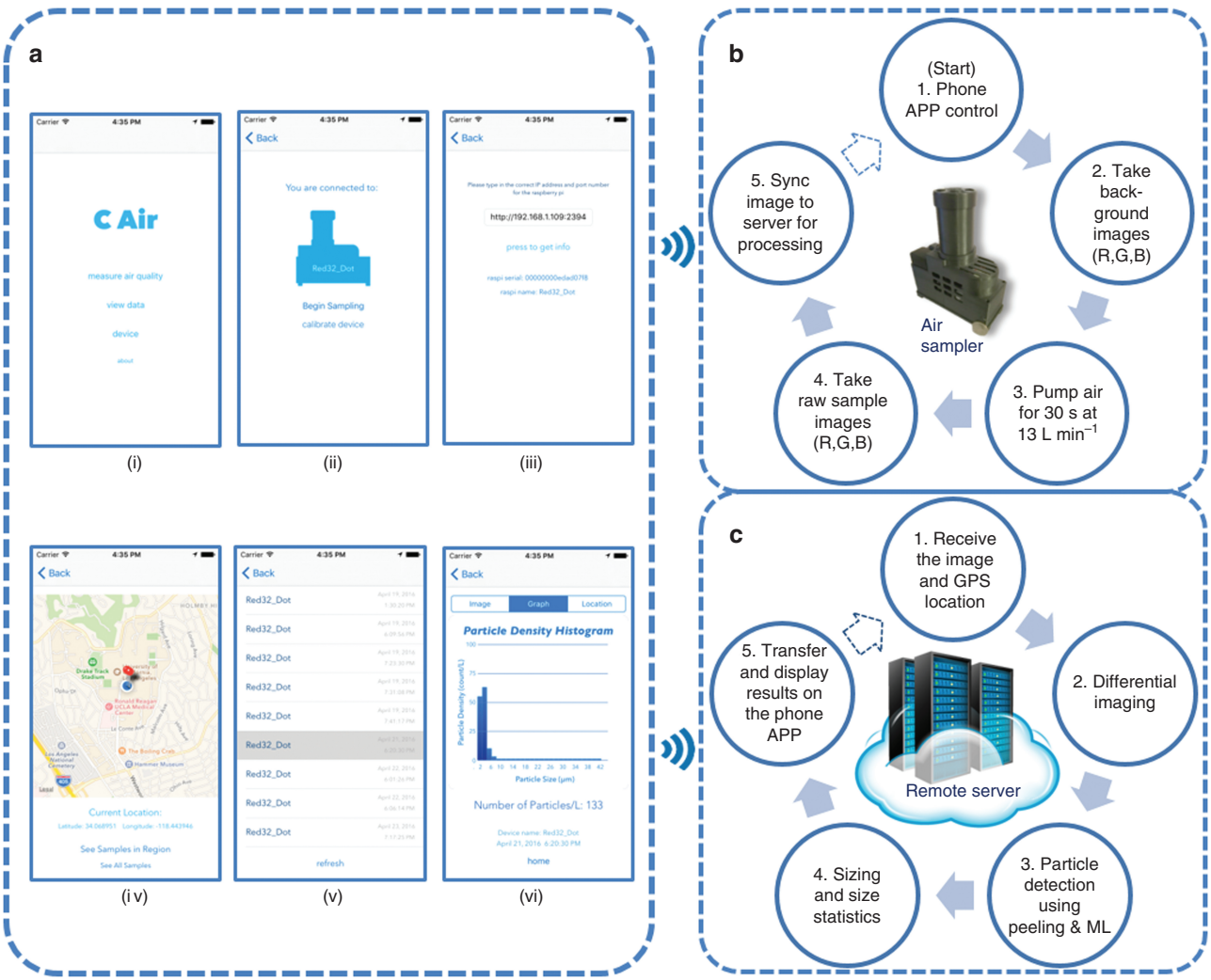

Figure 2 c-Air work flow and iOS-based app interface. (**a**) iOS-based c-Air app interface: (i) 'Welcome' screen of the app with different options. (ii) 'Take Measurement' screen with a device-logo-shaped sampling button. (iii) Changing the device connection. The user can change the device to be connected by typing the IP address of the device. (iv) 'Map View' of history samples. The air samples can be viewed by touching the pinpoint. (v) 'List View' of history samples. Each entry is a sample that shows the device name and capture time. (vi) View of one sample result. The 'graph' option shows a histogram of the particle sizing. (**b**) Work flow on the c-Air device. (**c**) Workflow on the server to support the processing of air samples. After the sample image and GPS location are sent to the server, the server processes the images through all five stages and saves the processed result. A copy of the result is sent to the smartphone app, where it is rendered and displayed. GPS, global position system; ML, machine learning.

sizing distribution with a sizing accuracy of ~93%. This large throughput and accuracy are especially important for providing highly sensitive and rapid measurements of particle counts at low concentrations in air.

By measuring the air quality using c-Air over several hours at an EPA-approved air-quality monitoring station, we confirmed that the c-Air PM measurements closely matched those of an EPA-approved BAM device. We further tested c-Air prototypes in various indoor and outdoor locations in California. In some of these experiments, a significant increase in ambient PM caused by the so-called Sand Fire near Santa Clarita, California on July 23, 2016 was detected. Finally, we conducted a 24-h spatiotemporal mapping of air pollution near Los Angeles International Airport (LAX) using the c-Air prototypes. The results revealed the occurrence of a temporal modulation of PM that correlates with the total number of flights at LAX. This modulation was present even at a distance of >7 km from LAX along the direction of landing flights. Because c-Air is based on computational microscopic imaging and machine learning, it can adaptively learn and potentially be tailored to sensitively recognize specific sub-groups of particles, including various types of pollen and mold, based on their phase and amplitude images, created by lens-free holographic imaging. We thus believe that the c-Air platform and its unique capabilities are broadly applicable to numerous air-quality-related applications, and it can provide cost-effective, compact and mobile solutions for spatio-temporal mapping of both indoor and outdoor air quality.

MATERIALS AND METHODS

Impaction-based air-sampler

To capture aerosols, we employ an impaction-based air sampler (that is, an impactor) on account of its high-throughput, simple hardware and compatibility with microscopic inspection[15]. As shown in Figure 1d, the impactor consists of an impaction nozzle and a sticky sampling coverslip (Air-O-Cell Sampling Cassette, Zefon International, Inc.). A pump drives the laminar airstream through the nozzle at high speed. The sticky coverslip is placed to directly face the airstream. The airstream can be easily redirected while the aerosol inside the stream impacts with and is collected by the sticky coverslip. This collection is subsequently used for computational imaging.

The aerosol capture by the impactor is actually a random process. The probability that an individual aerosol particle passing through the impactor will be captured depends on the particle size, laminar airflow rate and nozzle width. This probability is related to the Stokes number (Stk):[11]

$$Stk = \frac{\rho_P d_P^2 U C_c}{9\eta D_j} \tag{1}$$

where ρ_P is the particle mass density, d_P denotes the particle diameter, U represents the flow velocity, η is the air viscosity, D_j denotes the nozzle diameter and C_c is the slip correction coefficient. The impaction efficiency increases as Stk increases. On the basis of the same terminology, the cutoff size, d_{50}, is defined as the diameter of the particle at which the impaction efficiency decreases to 50%. In our experimental design, the air sampler (with a nozzle of 1.1 mm by 14.5 mm) was connected to and driven by a miniaturized pump with a throughput of 13 $L \cdot min^{-1}$. On the basis of the above relationship and assuming $\rho_P = 1\ 000\ kg \cdot m^{-3}$, our 50% cutoff sampling diameter can be estimated as $d_{50} = 1.4\ \mu m$ (Ref. 16).

c-Air lens-free on-chip microscope and air sampling design

For rapid imaging and inspection of the collected aerosols, we combined the impactor with a lens-free microscope, as shown in Figure 1. Similar to a typical lens-free imaging setup, the sticky coverslip, which was the sample to be imaged, together with the impactor nozzle cartridge, was directly placed on a color complementary metal-oxide semiconductor (CMOS) image sensor at a distance of approximately 400 μm from the image sensor to the sticky coverslip. Three fiber-coupled light-emitting diodes (LEDs; red: 624 nm; green: 527 nm; blue: 470 nm) were fixed on top of the device sampler tube at ~8 cm from the image sensor chip. Using LED illumination, the aerosol samples, which were captured by the sticky coverslip, cast in-line holograms. These holograms were recorded by the CMOS image sensor for holographic reconstruction and further processing to determine the PM statistics. Owing to the close proximity of the particles to the sensor surface, both the spatial and temporal coherence of the source could be partial, thereby eliminating the need for laser-based illumination[17].

The image capturing and air sampling processes are illustrated in Figure 2b. When the user makes the request to 'capture a sample' from the app interface, the three LEDs are sequentially turned on/off and three background images are thereby obtained. These background images depict the state of the air-sampler surface prior to the intake of the air to be sampled. On the basis of the coverage of the particles in a given background image, the device alerts the user for replacement of the air sampler surface. Depending on the level of air contamination, the same air sampler can be used several times before requiring replacement based on the contamination of its surface area.

Next, the pump was powered on to push the air through the sampler for 30 s, thereby screening 6.5 L of air. The three LEDs were then sequentially turned on/off, and three sample images were thereby obtained with the newly captured aerosol particles. These background images and sample images were both synced to the server for further processing. In this approach, we obtained two sets of images (that is, before and after sampling) to employ a differential imaging strategy. Specifically, after subtraction of the sample image from its corresponding background image, a differential hologram was formed, which contained the information of only the newly captured particles. For particle sizing, we used only the images captured under the green LED illumination. By merging all the differential holographic images captured using the three LEDs, red–green–blue color images of the captured particles could also be obtained, revealing the color information of the specimen, if desired. To avoid awaiting completion of the steps before a new sample could be obtained, we programmed the sampling process in a parallel approach. Accordingly, when a new sampling request arrived before the previous result was synced, the un-synced sample was cached first. It was later synced when the device became idle. The entire device sampling process was controlled by a custom-developed program on a microcomputer (Raspberry Pi A+), along with a custom-designed circuit (Supplementary Fig. S1). If stand-alone operation of the device (without any data connectivity) is preferred in some applications, the same Raspberry Pi microcomputer that we are currently using as the controlling board in our design can provide sufficient computational power for image reconstruction and particle analysis, once the image processing algorithms are transferred from Matlab into C++-based codes.

Particle detection using digital 'peeling'

Direct back-propagation of the acquired hologram (Supplementary Equation (S1)) to the auto-focused sample plane generates a spatial artifact, called the twin-image noise, on top of the object. This twin-

doi:10.1038/lsa.2017.46

image artifact affects the detection of aerosol particles. If left unprocessed, it can lead to false-positives and false-negatives. To address this problem, we employ an iterative particle peeling algorithm[18] in our holographic reconstruction process. It is additionally combined with a support vector machine (SVM)-based learning model to further reject these spatial artifacts. The algorithm is summarized as a flowchart in Supplementary Fig. S2.

This peeling algorithm contains four cycles of detection and erasing ('peeling out') of the particles at progressively increasing thresholds, that is, 0.75, 0.85, 0.92 and 0.97, where the background is centered at 1.0 during the differential imaging process (Supplementary Information). The highest threshold (0.97) is selected as 3σ from the background mean, where $\sigma \approx 0.01$ is the s.d. of the background. We use a morphological reconstruction process[19] to generate the image mask instead of using a simple threshold. Because most particles have a darker center and a somewhat weaker boundary, using a single threshold may mask parts of the particle, potentially causing the particle to be missed or re-detected multiple times in subsequent peeling cycles. This is avoided by using a morphological reconstruction process.

In each cycle of this digital particle peeling process, we first adjust the image focus using the auto-focusing algorithm (Supplementary Information). Then, a morphological reconstruction is employed to generate a binary mask, where each masked area contains a particle. For each mask, we crop a small image (100×100 pixels) and perform fine auto-focusing on this small image to find the correct focus plane of the corresponding particle. At this focus plane, we extract various spatial features of the particle, for example, minimum intensity I_m, average intensity I_a, area A and maximum phase θ_M. We then propagate (using Supplementary Equation (S1)) the image to five different planes uniformly spaced between 20 μm above and 20 μm below this focus plane. The Tamura coefficient (see Supplementary Equation (S3)) of this focus plane is calculated and compared to the coefficients of these five other planes. The ratio of the Tamura coefficient at this focus plane against the highest Tamura coefficient of all six planes is defined as another feature, R_{Tam}. These four features, I_m, θ_M, A and R_{Tam}, are then fed into an SVM-based learning model to digitally separate spatial artifacts from true particles and reject such artifacts. This learning algorithm is detailed in the following subsection. After all the detected particles in this peeling cycle are processed, we digitally peel out these 'counted' particles, that is, replace the thresholded area corresponding to each detected particle with the background mean, on both the image and twin image planes. We then move to the next peeling cycle with a higher threshold and repeat the same steps.

After completing all four peeling cycles, the extracted features, I_m, θ_M and A, are further utilized for particle sizing using a machine-learning algorithm, as detailed further below. This sizing process is only performed on true particles, which generates a histogram of particle sizes and density distributions, as well as various other parameters, including, for example, total suspended particulate (TSP), PM10 and PM2.5, reported as part of c-Air result summary.

Elimination of false-positives using a trained support vector machine

To further avoid false-positives in our detection system, we used a trained linear SVM that is based on four features, I_m, θ_M, A and R_{Tam}, as described in the previous sub-section, to distinguish spatial artifacts from true particles and increase c-Air detection accuracy. These spatial features were selected to provide the best separation between the true- and false-particles. To train this model, we obtained two air sample images using a c-Air prototype, one indoor and one outdoor. Then, in addition to our c-Air-based analysis, we physically extracted the sampling coverslip and inspected the captured particles under a benchtop bright-field microscope using a $40\times$ objective lens. We compared the thresholded areas in our peeling cycle and lens-free reconstruction process with the images of the benchtop microscope to mark each one of these detected areas as a true particle or a false one. Using this comparison, we labeled a total of >2000 thresholded areas and fed half of this training data into our SVM model[20] (implemented in Matlab using the function 'svmtrain'). The other half was used for blind testing of the model, which showed a precision of 0.95 and a recall of 0.98.

Machine-learning-based particle detection and sizing

We used a custom-designed machine-learning algorithm trained on size-calibrated particles to obtain a mapping from the detected spatial characteristics of the particles to their diameter, also helping us avoid false positives, false negatives as well as over-counting of moved particles in our detection process. For this purpose, we used some spatial features extracted from the holographic particle images, including for example, minimum intensity I_m, average intensity I_a and area A, and developed a second-order regression model that maps these features to the sizes of the detected particles in microns. The model is deterministically learned from size-labeled particle images, which are manually sized using a standard benchtop microscope. Specifically, after we extract features I_m, I_a and A of the masked region in a particle peeling cycle, we strive to find a model, f, that maps these features to the particle diameter D in microns, that is,

$$D = f\left(I_m, I_a, \sqrt{A}\right) \tag{2}$$

Where f can potentially have infinite dimensions. However, we employ a simplified second-order polynomial model of f and extend the features to the second-order by defining:

$$X = \left[1, I_m, I_a, \sqrt{A}, I_m^2, I_a^2, A, I_m I_a, I_m\sqrt{A}, I_a\sqrt{A}\right] \tag{3}$$

We then define a linear mapping, θ, that relates the second-order features to the diameter of the particle:

$$D = f\left(I_m, I_a, \sqrt{A}\right) = \theta^T \hat{X} = \theta^T\left(\frac{X-\mu}{\sigma}\right) \tag{4}$$

where T refers to the transpose operation, and μ and σ represent the mean and s.d. of X, respectively.

Based on the above mapping, we used 395 size-labeled microbeads for training and blind testing. These polystyrene microbeads ranged in diameter from ~1 to ~40 μm, as shown in Figure 3. The ground truth sizes of these particles were manually measured under a benchtop microscope with a $100\times$ 0.95 numerical aperture (NA) objective lens. The same samples were additionally imaged using the c-Air platform to obtain the corresponding lens-free images and extract spatial features, I_m, θ_M and A. For training the machine-learning model, we first randomly and evenly separated the microbead samples into respective training and testing sets. After extending the features to the second-order (Equation (3)) and performing normalization (Equation (4)), we fitted the parameter vector θ by minimizing the difference between the training feature mapping $\left(\theta^T \hat{X}_{tr}\right)$ and the calibrated diameter $\left(D_{tr}^{mic}\right)$ that is,

$$\min_\theta \|\theta^T \hat{X}_{tr} - D_{tr}^{mic}\|_1 \tag{5}$$

This minimization was performed by CVX, a software package designed for solving convex optimization problems[21]. The same

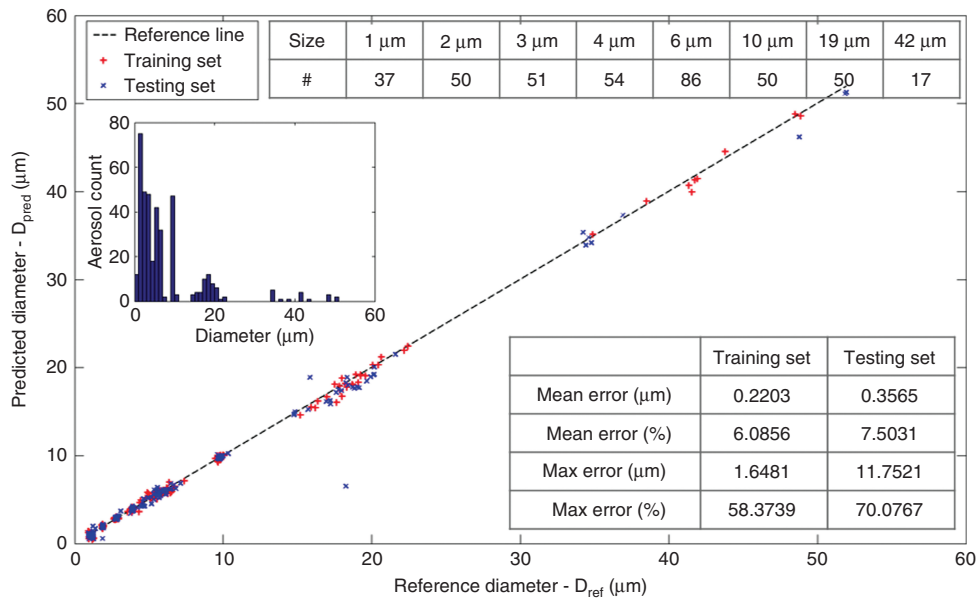

Figure 3 Machine-learning-based particle detection and sizing with high accuracy using c-Air. The designated bead sizes are shown in the uppermost table. The microscope-calibrated size distribution is plotted as the histogram within the large figure. The large figure in the background shows the machine-learning mapped size (D_{pred}) using c-Air. It is compared to the microscope-measured size (D_{ref}) for both training and testing sets. The middle dashed line represents $D_{pred} = D_{ref}$. The sizing error, which is defined by Equations (6) to (7), is shown in the lower-right table in both µm and the relative percentage. A ~93% accuracy using machine-learning-based sizing is demonstrated.

trained parameter was then applied for the cross-validation set, which was comprised of another 197 microbeads. Particle sizing training errors (E_{tr}) and testing errors (E_{cv}) were validated by evaluating the norm of difference:

$$E_{tr} = \|\theta^T \hat{X}_{tr} - D_{tr}^{mic}\|_p \quad (6)$$

$$E_{cv} = \|\theta^T \hat{X}_{cv} - D_{cv}^{mic}\|_p \quad (7)$$

where $\theta^T \hat{X}_{cv}$ is the testing feature mapping, and D_{cv}^{mic} is the calibrated diameter for the testing set. In addition, $p = 1$ is used for calculating the 'mean error,' and $p = \infty$ is used for calculating the 'maximum error.' Note that this training process only needs to be done once, and the trained parameter vector, θ and the normalization parameters, μ and σ, are then saved and subsequently used for blind particle sizing of all the captured aerosol samples using c-Air devices.

RESULTS AND DISCUSSION

C-Air platform spatial resolution, detection limit and field of view

The USAF-1951 resolution test target was used to quantify the spatial resolution of the c-Air platform. The reconstructed image of this test target is shown in Supplementary Fig. S3, where the smallest resolvable line is group eight, element two (line width 1.74 µm), which is currently pixel-size limited due to our unit magnification imaging geometry[17,22]. If required in future applications, a better resolution (for example, ≤ 0.5 µm) can be achieved in our c-Air platform using a CMOS sensor with a small pixel size and/or by applying pixel super-resolution techniques to digitally synthesize smaller pixel sizes[22–25].

In our reconstructed lens-free differential images, we defined the detection noise floor as 3σ ($\sigma \approx 0.01$ is the s.d. of the background) from the background mean, which is always 1 in a given normalized differential image, as detailed in our Supplementary Information. For a particle to be viewed as detected, its lens-free signal should be above this 3σ noise floor. As shown in Supplementary Fig. S4, 1 µm particles can be clearly detected, which is also cross-validated by a benchtop microscope comparison. We should note that, as desired, this detection limit is well below the 50% cut-off sampling diameter of our impactor ($d_{50} = 1.4$ µm, see the Materials and Methods section for details).

In terms of the imaging field of view, the active area of the CMOS sensor in our c-Air design is $3.67 \times 2.74 = 10.06$ mm^2. However, in the impactor air sampler geometry (Figure 1d), the particles are deposited immediately below the impaction nozzle. Thus, the active area that will be populated by aerosols and imaged by the lens-free microscope will be the intersection of the active area of the CMOS sensor and the impaction nozzle opening. Because the slit has a width of only 1.1 mm, the resulting effective imaging field of view of c-Air is $3.67 \times 1.1 = 4.04$ mm^2. With either the selection of a different CMOS image sensor chip or a custom-developed impaction nozzle, the nozzle slit area and the image sensor area can have larger spatial overlaps to further increase this effective field of view in future c-Air designs.

Particle-sizing accuracy using machine learning

As detailed in the Materials and Methods section, we used a machine-learning algorithm trained on size-calibrated particles to obtain a mapping from the detected spatial characteristics of the particles to their diameter. Figure 3 depicts how well the predicted particle diameter, D_{pred}, based on our machine-learning algorithm described in the Materials and Methods section, agrees with the ground-truth measured diameter, D_{ref}. The sizing errors for training and testing sets are defined in Equations (6) and (7), respectively. The dotted black line in Figure 3 represents the reference for $D_{ref} = D_{pred}$. As shown in Figure 3, using machine learning, c-Air achieved an average sizing error of ~7% for both the training and blind testing sets. For non-standard particles, for example, rod-shaped or arbitrarily shaped fibers, our microscopic imaging system will be able to determine that the above described size mapping will not be applicable. For these non-standard particles that are detected on our sampling surface, we can characterize them using new parameters based on their

doi:10.1038/lsa.2017.46

reconstructed images, such as eccentricity, length, width and area. In fact, this forms another advantage of our approach since it can also report the concentrations of such non-standard particles, along with their phase and amplitude images at different wavelengths, which other existing techniques cannot.

Particle size distribution measurements and repeatability of the c-Air platform

We employed two c-Air devices, which were designed to be identical, and we conducted repeated measurements at four locations: (1) the class-100 clean room of California NanoSystems Institute (CNSI) on 21 June 2016; (2) the class-1000 clean room at CNSI on 23 May 2016; (3) the indoor environment in the Engineering IV building at the University of California, Los Angeles (UCLA) campus on 25 May 2016; and (4) the outdoor environment at the second floor patio of the Engineering IV building on 23 May 2016. At each location, we obtained seven samples for each c-Air device with a sampling period of 30 s between the two successive measurements. These sample c-Air images were processed as described in the Materials and Methods section, and the particle size distributions for each location were analyzed and compared.

Figure 4a–4c shows a box-whisker plot of the data distribution for TSP, PM10 and PM2.5 at these four locations. The points, marked by an 'x' symbol, were excluded as outliers from the box plot with a whisker length of 1.5 (99.3% confidence). The mean and s.d. of the seven measurements in each of the four locations are summarized in Supplementary Table S1. It is interesting to note that c-Air measured the TSP density at ~7 counts per liter for the class-100 clean room

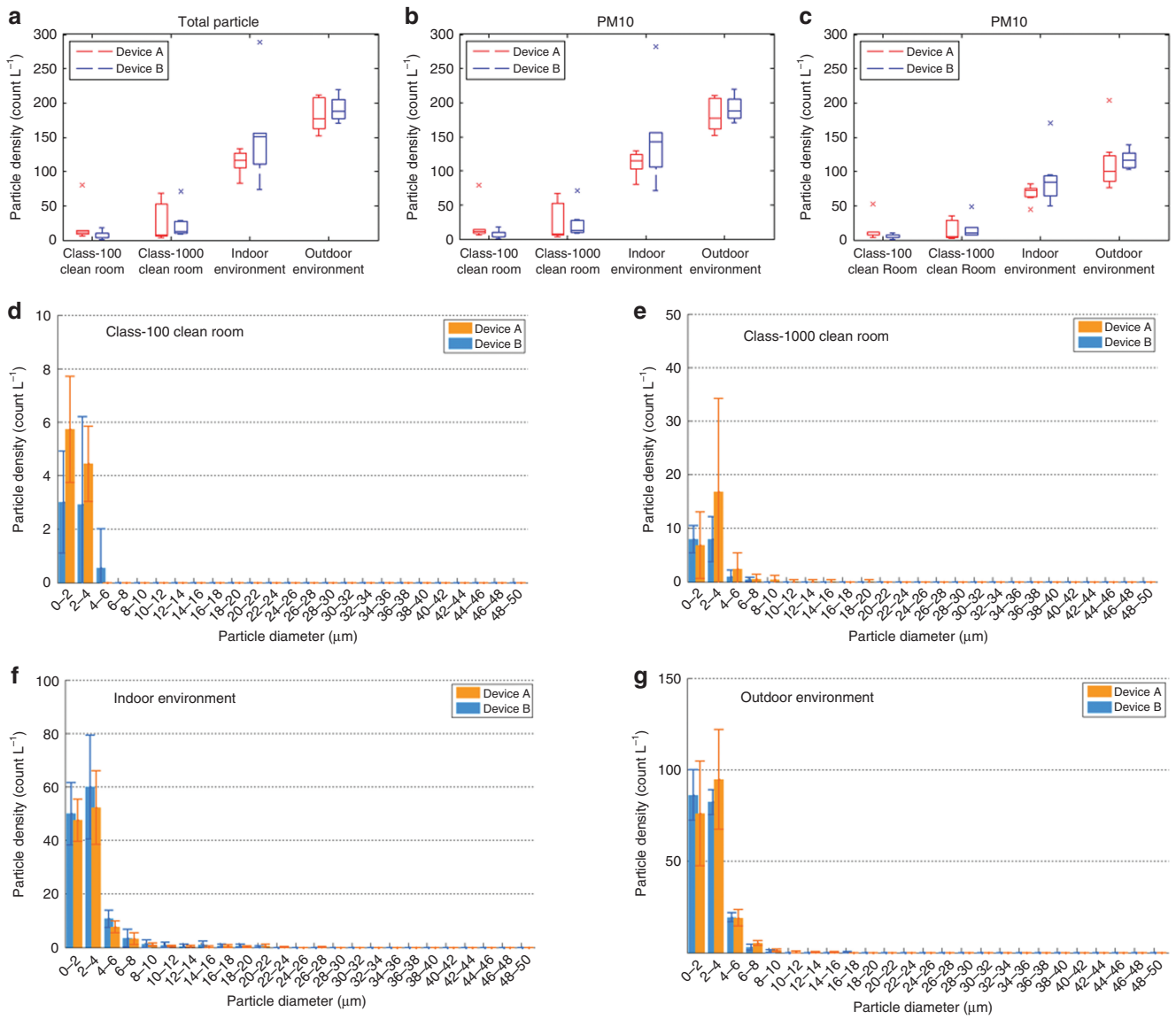

Figure 4 c-Air repeatability tests at different locations. (**a**–**c**) Box-plot of the repeatability test results using two c-Air devices (A and B) at the (1) class-100 clean room of CNSI on 21 June 2016; (2) class-1000 clean room at CNSI on 23 May 2016; (3) indoor environment of the UCLA Engineering IV building on 25 May 2016; and (4) outdoor environment at the second floor patio of the UCLA Engineering IV building on 23 May 2016. The box-plot was generated using the box-whisker plot method with a whisker length of 1.5 (99.3% confidence) to exclude outliers, which are marked by the symbol 'x.' (**d**–**g**) Particle size and density distribution histogram comparison at each location: **d** Class-100 clean room; **e** class-1000 clean room; **f** indoor environment; and **g** outdoor environment. Seven samples for each c-Air device with a sampling period of 30 s were obtained at each location.

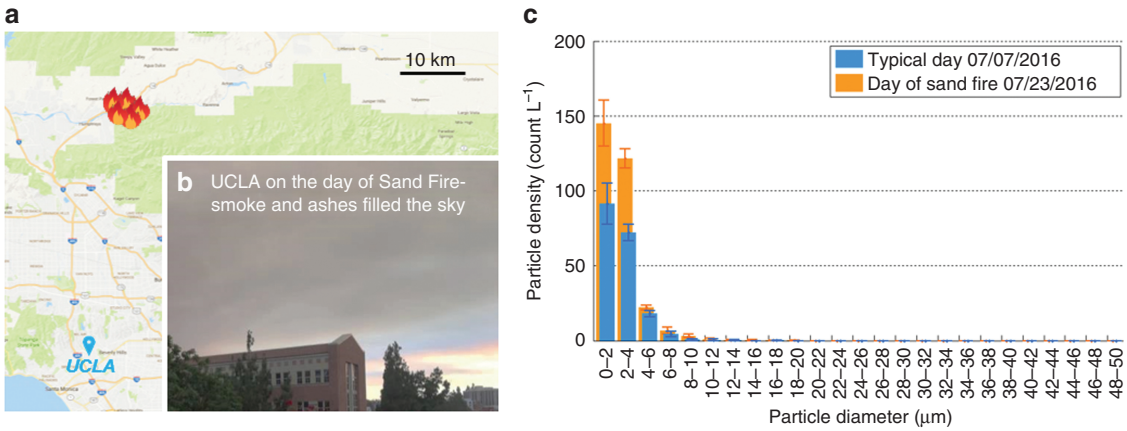

Figure 5 Particle size and density of the UCLA outdoor environment affected by the Sand Fire on 22 July 2016. (**a**) Map showing the area struck by the Sand Fire on 22 July 2016 to 23 July 2016. UCLA is also pinpointed on the map; it is more than 40 km from the fire location. (**b**) A photograph taken at around 5:00 pm from the second floor patio of the UCLA Engineering IV building. (**c**) Histogram comparison of the sample measured on a regular day, 07/07 at around 4:00 pm and the day of the Sand Fire, 07/22 at around 5:00 pm, at the same location using c-Air. Each histogram bar plot with a s.d. bar was generated from six 30-s samples. The background map of **a** is cropped from Ref. 33.

and 25 counts per liter for the class-1000 clean room at CNSI, which are both comparable to the ISO 14644-1 clean room standards[26], that is, 3.5 counts per liter for the class-100 clean room and 36 counts per liter for the class-1000 clean room for particles ≥0.5 μm.

The measurements of TSP, PM10 and PM2.5 densities from the same data set was additionally used to elucidate two aspects of the repeatability of the c-Air platform, that is, the intradevice and interdevice repeatability. The intradevice repeatability is defined as the extent to which the measurement result varies from sample to sample using the same c-Air device to measure the air quality in the same location (assuming that the air quality does not change from measurement to measurement with a small time lag in between). The strong intradevice repeatability of c-Air is evident in the 'max–min' perspective in the box plot of Figure 4a–4c, or as the s.d. (std, σ) in Supplementary Table S1.

The interdevice repeatability is defined as the extent to which the results vary from each other using two c-Air devices that are designed as identical to measure the air quality in the same location. This can be qualitatively viewed by comparing the measurement result of device A and device B in Figure 4. To further quantify the interdevice repeatability, we performed a μ-test (that is, Mann–Whitney μ-test or Wilcoxon rank sum test) on the 2×4 sets of measurement data from devices A and B at four different locations. In the μ-test, we aimed to verify the null hypothesis ($H=0$) for two sets of samples, X and Y:

$$H = 0 : P(X > Y) = P(Y > X) = \frac{1}{2} \tag{8}$$

That is, we strived to test if the medians of the two samples are statistically the same. Compared to other tests for repeatability, for example, the student t-test, the μ-test requires fewer assumptions and is more robust[27]. We thus used a Matlab built-in function, *ranksum*, to perform the μ-test and the hypothesis results and prominent P-values are summarized in Supplementary Table S2. As shown in this table, the null hypothesis $H=0$ is valid for all the 2×4 sets of measurement data (from devices A and B at four different locations), showing the strong inter-device repeatability of our c-Air platform.

c-Air measurements showing Sand Fire incident influence at >40-km distance

On 22 July 2016, the so-called Sand Fire struck near the Santa Clarita region in California and remained uncontained for several days[28,29]. Figure 5a marks both the locations of this wild fire and the UCLA campus. Although UCLA was more than 40 km from the location of the fire, on 23 July around noon, smoke and ashes filled the sky near UCLA, as shown in the photo of Figure 5b. We obtained six air samples using the c-Air device at an outdoor environment at UCLA, as described in the above sub-section. We compared the results with a previous sample obtained on a typical day, 7 July 2016, using the same device and at the same location. The data of both days contained six 30-s air samples measured with c-Air, with a ~2-min interval between the successive samples. For each day, the particle size distributions of the six samples were averaged and the s.d. were plotted as the histogram in Figure 5c. The results showed that the outdoor PM density significantly increased on the day of the wild fire, especially for particles smaller than 4 μm, which showed an approximately 80% increase. This increase in the density of smaller particles is natural because comparatively smaller particles can travel this long distance (>40 km) and still have significant concentrations in air.

Comparison of c-Air with a standard BAM PM2.5 instrument

On 16 August 2016, we employed a c-Air device at the Reseda Air Quality Monitoring Station (18330 Gault St, Reseda, CA, USA) and obtained a series of measurements during a 15-h period starting from 6:00 am. We compared the performance of the c-Air device with that of the conventional EPA-approved BAM PM2.5 measurement instrument (BAM-1020, Met One Instruments, Inc.).

The EPA-approved BAM-1020 pumps air at ~16.7 L·min^{-1} and has a rotating filter amid airflow that accumulates PM2.5 to be measured every hour. A beta-particle source and detector pair inside measures the attenuation induced by the accumulated PM2.5 on the filter and converts it to total mass using the Beer–Lambert law. The quantity reported from BAM-1020 is hourly averaged PM2.5 mass density in μg·m^{-3}. In comparison, the c-Air device is programmed to obtain a 30-s average particle count per 6.5 L of air volume. It performs sizing and concentration measurements using optical microscopic imaging, as detailed in the Materials and Methods section.

doi:10.1038/lsa.2017.46

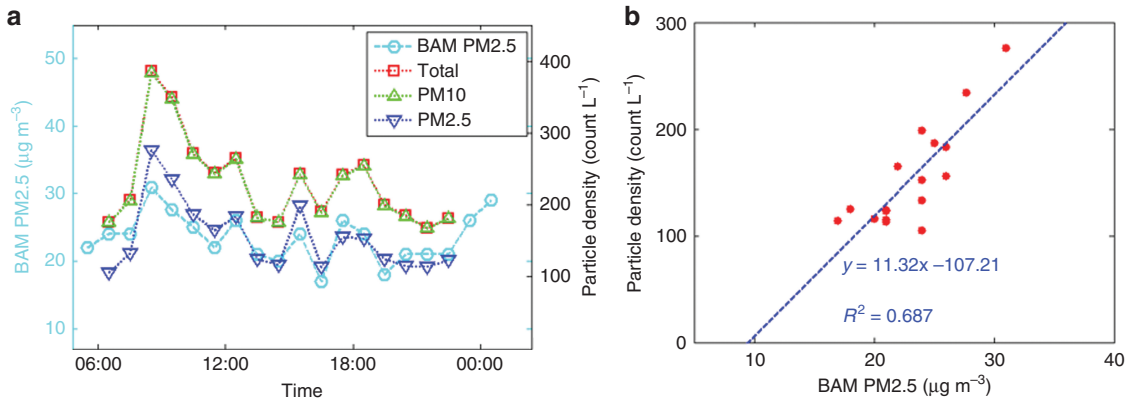

Figure 6 Comparison of c-Air results against a standard BAM PM2.5 instrument. (**a**) Superimposed hourly plot of (right axis) particle density counted by a c-Air device, and (left axes) hourly accumulated PM2.5 total mass density measured by the standard BAM PM2.5 instrument at the Reseda Air Sampling Station. (**b**) Linear correlation plot of PM2.5 hourly average count density measured by c-Air (*y* axis) with a PM2.5 hourly average mass density measured by BAM-1020 PM2.5 measurement device (*x* axis). The BAM-PM2.5 data were downloaded from Ref. 30.

To enable a fair comparison, we obtained four 30-s measurements every hour, with 10- to 15-min intervals between consecutive c-Air measurements. We measured the PM2.5 densities corresponding to these samples and obtained their average as our final measured PM2.5 density for a given hour. This c-Air average was compared to the hourly average PM2.5 mass density measured by BAM-1020. The measurements of the c-Air device were obtained on the roof of the Reseda Air Sampling Station close to the inlet nozzle of BAM-1020; however, it was situated ~2 m from it to avoid interference between the two systems.

Figure 6 plots the comparison of the measurement results from this c-Air device and BAM-1020. As shown in Figure 6a, c-Air's hourly average PM2.5 count density result (blue curve) closely follows the same trend as the EPA-approved BAM PM2.5 mass density result (cyan curve). We also plotted hourly averaged TSP (red curve) and PM10 (green curve) in the same Figure 6a, which follows a similar trend as PM2.5. Last, we found a linear correlation between the BAM PM2.5 measurements and c-Air PM2.5 count density measurements, as shown in Figure 6b, where the *x* axis is the PM2.5 mass density in $\mu g \cdot m^{-3}$ measured by the BAM-1020, and the *y* axis is the PM2.5 count density in counts per liter measured by the c-Air device. Some of the variations between the two techniques may be due to several reasons: (1) Each PM2.5 particle may have a different weight; therefore, the PM2.5 count density may not directly convert to mass density of the particles; (2) There may be some air-quality variations within every hour; thus, our four 30-s measurements may not accurately represent the whole hourly average reported by BAM-1020; (3) The cutoff size of our impactor is ~1.4 μm, which means particles smaller than this size may not be efficiently counted by our device, whereas they are counted by BAM-1020.

Note also that, in Figure 6a at 7:00 to 9:00 am, the original measurements by BAM-1020 are missing on account of the replacement of the rotating filter, which is required for the instrument's maintenance. Instead, these data points are replaced by the average of the 7:00 to 9:00 am time windows on Fridays, which were measured within the same month (Supplementary Fig. S5 and Ref. 30).

Spatial-temporal mapping of air-quality near LAX

On 6 September 2016, we employed two c-Air devices, device A and device B, to measure the spatio-temporal air quality changes around LAX. To this end, we obtained two 24-h measurements spanning two different routes that represent the longitudinal and latitudinal directions, which were centered at LAX (Figures 7 and 8). We selected six locations in each route and performed measurements with a period of 2 h in each route over 24 h. These raw c-Air measurements were sent to our server for automatic processing to generate the particle size statistics at each time and location.

Route 1 extended from LAX to the east in a longitudinal direction, as shown in Figure 7a. Along this route, we selected six sites that were located at 3.37, 4.34, 5.91, 7.61, 9.95 and 13.1 km east of LAX, respectively. LAX shows a pattern of a large number of flights throughout the day (7:00 am to 11:00 pm); however, it shows a prominent valley at late night (around 2:00 am), where the number of flights is minimal, as shown by the cyan curves in Figure 7a. As depicted in bubble boxes (1) to (6) in Figure 7a, the c-Air measurement results of both PM2.5 and PM10 also show such a valley during late night, which illustrates the relationship between the total number of flights at LAX and the nearby PM pollutants. As the distance increases from LAX, this modulation weakens. To quantify this correlation, we defined two measures: (1) the correlation slope, which is the slope of the linear mapping from the total number of flights to the PM10 or PM2.5 count density (plotted as a function of the longitudinal distance from LAX in Figure 7b), and (2) the daily average PM measured by c-Air, which is the 24-h average PM10 or PM2.5 count density for each location (also plotted as a function of the longitudinal distance from LAX in Figure 7c). These figures show an exponential trend for both the correlation slope and the daily average PM as a function of the distance from LAX. Moreover, they indicate that the impact of the airport in increasing air pollution is significant, even >7 km from its location. This has also been independently confirmed in earlier studies[31], using a commercially available optical scattering based PM detection technology[10] that has a limited dynamic range of particle size and density, and more than an order of magnitude lower throughput compared to ours due to its serial read-out scheme as discussed in our Introduction section. Note also that there is an unexpected point at the third location (5.91 km from LAX), which seems to have a higher pollution level above the exponential trend that is observed. We believe this is due to the existence of a parking lot of ~3400 car spaces and a related construction site in <65 m to this measurement location (Supplementary Fig. S6).

Unlike Route 1, Route 2 extended from the south to the north of LAX, spanning a latitudinal direction. The six locations chosen in this

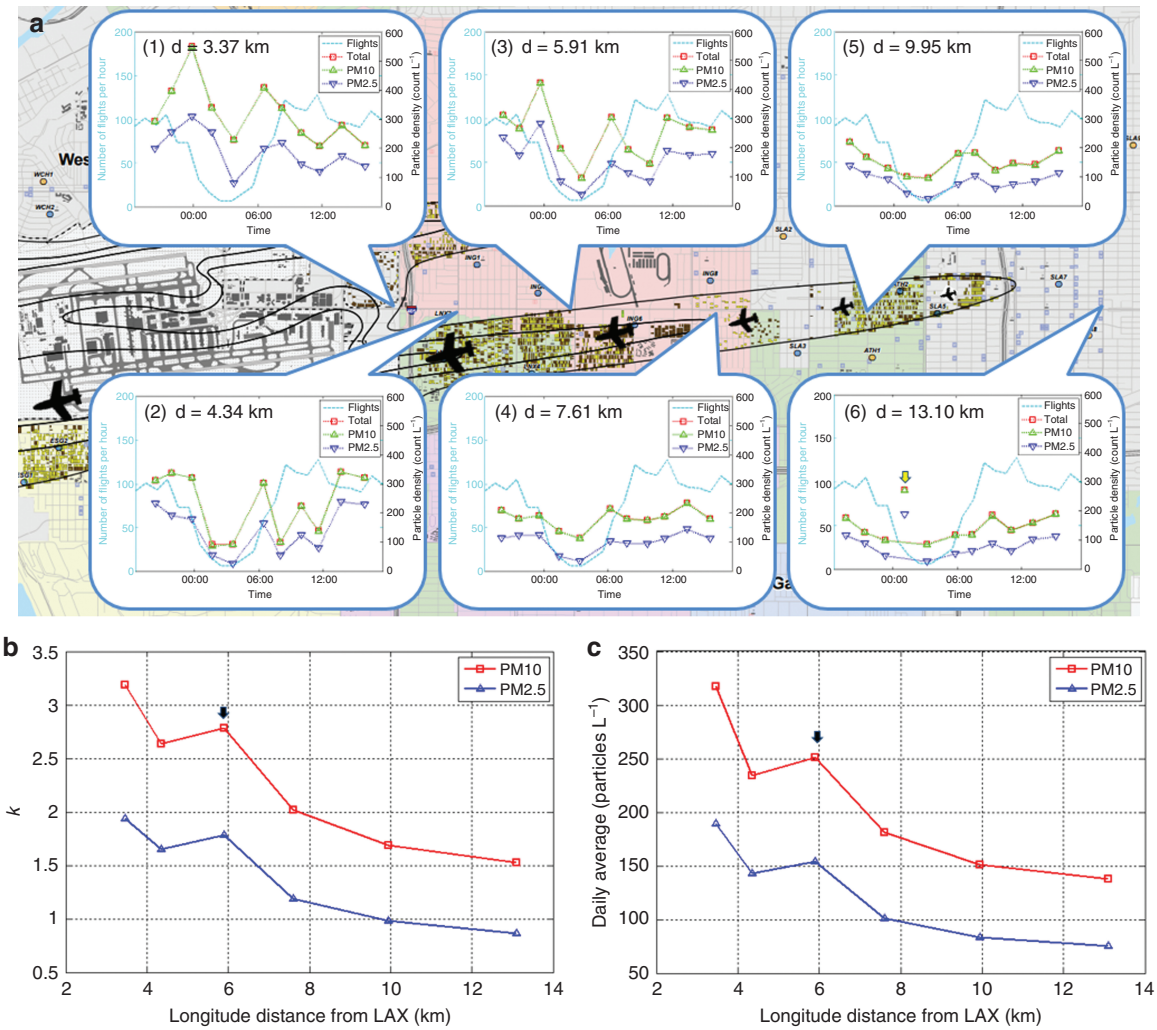

Figure 7 LAX measurements in the longitudinal direction using c-Air. (**a**) Noise map near LAX. The east side of LAX is where airplanes arrive; it is marked by tiny airplane icons. We obtained a 24-h PM measurement on 06 Spetember 2016 to 07 September 2016 at the following locations: (1) 5223 W. Century Blvd., (2) 10098 S. Inglewood Ave., (3) 4011 W. Century Blvd., (4) 3000 W. Century Blvd., (5) 1407 W. 101st St and (6) 9919 S. Avalon Blvd., as marked on **a**. The fourth time point at location (a-6) was excluded from the curve because there was a large water sprinkler turned on during the measurement, which affected the c-Air performance. (**b**) Correlation slope plotted for locations (1–6) as a function of their longitudinal distances from LAX. (**c**) Daily average PM plotted for locations (1–6) as a function of their longitudinal distances from LAX. The third point in **b** and **c**, as marked by a black arrow, is inconsistent with the trend, which we believe is on account of the presence of an immense (~3400 spaces) parking lot nearby that specific measurement location (Supplementary Fig. S6). **a** depicts the noise maps of the second quarter of 2016 near LAX cropped from Ref. 34. The total number of flights, represented by the cyan curve of (a-1) to (a-6), is plotted from the data given by Ref. 35.

route were 3.58, 1.90, 0.50, 0.01, −1.46 and −2.19 km north of LAX, respectively. Similar to Route 1, bubble boxes (1) to (6) of Figure 8a plot the time variations of the PM concentration during the sampling points corresponding to Route 2. These results once again show a similar trend of PM variation in accordance with the total number of flights at LAX. Similar to Route 1, as the measurement location distance from LAX increases, the modulation strength diminishes. The above finding is supported by the correlation slope shown in Figure 8b and the daily average PM shown in Figure 8c, both of which are a function of the latitudinal distance north of LAX. We note that the decrease is more rapid in this latitudinal direction (south-to-north, Route 2) than the longitudinal direction (west-to-east, Route 1), which may be on account of the typical west winds near LAX during the summer, which cause the particles to travel longer distances in air[32].

CONCLUSIONS

In this paper, we demonstrated a portable and cost-effective PM imaging, sizing and quantification platform, called c-Air, which uses lens-free computational microscopy and machine learning. The platform consists of a field-portable device weighing ~590 g, a smartphone app for device control and display of results and a remote server for automated processing of digital holographic microscope images for PM measurements based on a custom-developed machine learning algorithm. The performance of the device was validated by measuring air quality at various indoor and outdoor locations, including an EPA-regulated air sampling station, where we compared c-Air results with those of an EPA-approved BAM device, and a close correlation was shown. We further used c-Air platform for spatio-temporal mapping of air-quality near LAX, which showed the PM concentration varying throughout the day in accordance with the total

doi:10.1038/lsa.2017.46

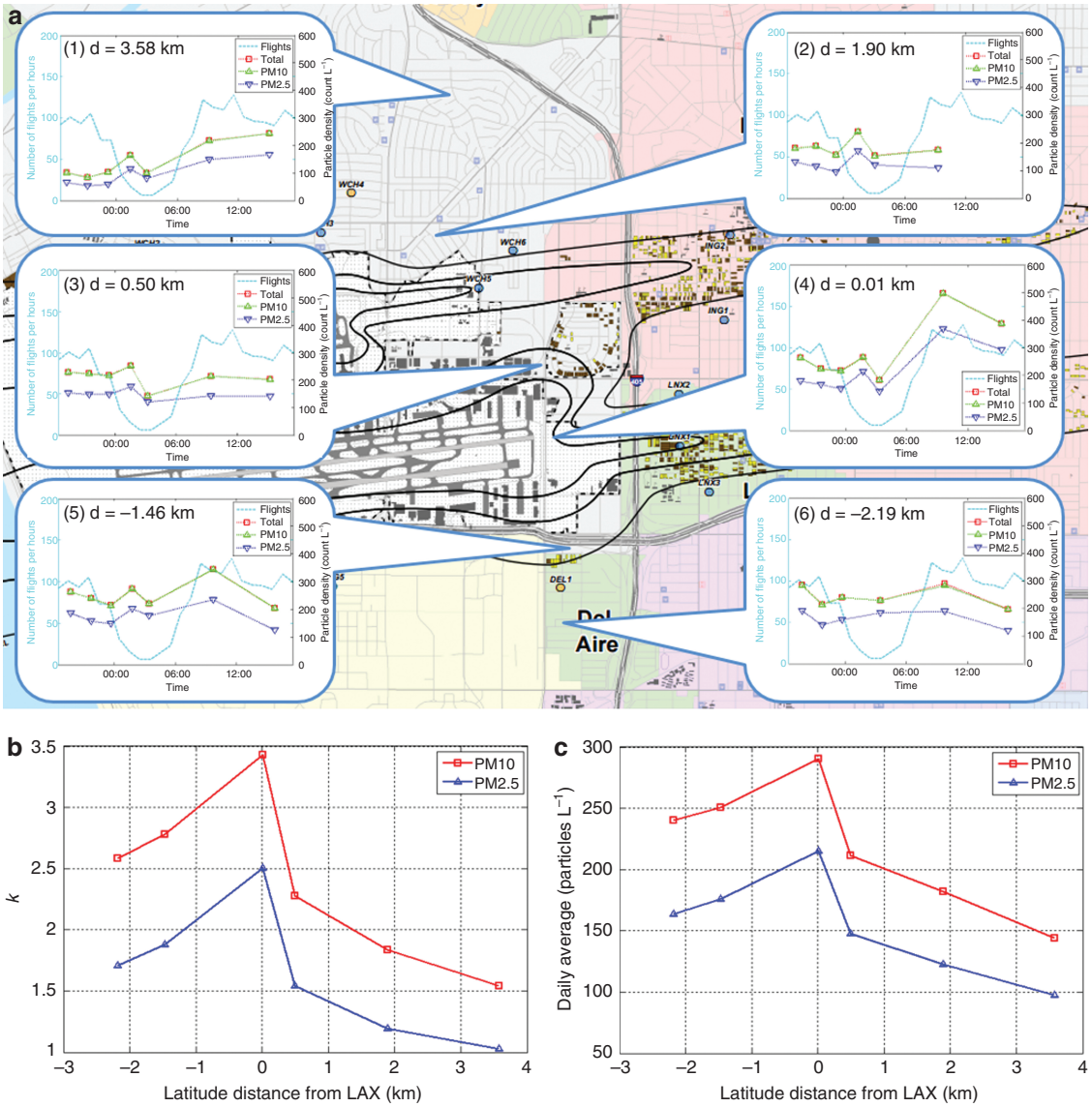

Figure 8 LAX measurements in the latitudinal direction using c-Air. (**a**) Noise map near LAX. We obtained a 24-h PM measurement on 09/06/2016–09/07/2016 at locations (1) 6076 W. 76th St, (2) 8701 Airlane Ave., (3) 5625 W. Century Blvd., (4) 10400 Aviation Blvd., (5) 5457 W. 117th St and (6) 5502 W. 122nd St, as marked on **a**. (**b**) Correlation slope plotted for locations (1–6) as a function of their latitudinal distances from LAX. (**c**) Daily average PM plotted for locations (1–6) as a function of their latitudinal distances from LAX. **a** is the noise map of the second quarter of 2016 near LAX cropped from Ref. 34.

number of flights at LAX. The strength of this correlation, as well as the daily average PM, exponentially decreased as a function of the increasing distance from LAX. We believe that the c-Air platform, with its microscopic imaging and machine learning interface, has a wide range of applications in air quality regulation and improvement.

CONFLICT OF INTEREST

AO is the co-founder of a company (Holomic/Cellmic LLC) that commercializes computational microscopy, sensing and diagnostics tools.

ACKNOWLEDGEMENTS

The Ozcan Research Group at UCLA gratefully acknowledges the support of the Presidential Early Career Award for Scientists and Engineers (PECASE), the Army Research Office (ARO; W911NF-13-1-0419 and W911NF-13-1-0197), the ARO Life Sciences Division, the National Science Foundation (NSF) CBET Division Biophotonics Program, the NSF Emerging Frontiers in Research and Innovation (EFRI) Award, the NSF EAGER Award, NSF INSPIRE Award, NSF Partnerships for Innovation: Building Innovation Capacity (PFI:BIC) Program, Office of Naval Research (ONR), the National Institutes of Health (NIH), the Howard Hughes Medical Institute (HHMI), Vodafone Americas Foundation, the Mary Kay Foundation, Steven & Alexandra Cohen Foundation and KAUST. This work is based upon research performed in a laboratory renovated by the National Science Foundation under Grant No. 0963183, which is an award funded under the American Recovery and Reinvestment Act of 2009 (ARRA). The authors also acknowledge the support of South Coast Air Quality Management District (AQMD) for their assistance in the experiment at Reseda Air Quality Monitoring Station, and Aerobiology Laboratory Association, Inc. in Huntington Beach, CA for providing experiment materials. YW also acknowledges Dr Euan McLeod and Dr Jingshan Zhong for helpful discussions. We also acknowledge Dr Yair Rivenson, Mr Calvin Brown, Mr Yibo Zhang, Mr Hongda Wang and Mr Shuowen Shen for their help with some of the c-Air measurements.

1 WHO. Ambient (outdoor) air quality and health. Available at: http://www.who.int/mediacentre/factsheets/fs313/en/ (accessed on 28 May 2016).
2 Wong E. *Smog So Thick, Beijing Comes to a Standstill*. New York Times, 2015.
3 Agence France-Presse in Beijing. Beijing's smog 'red alert' enters third day as toxic haze shrouds city. Guardian, (2015-12-21). Available at: http://www.theguardian.com/world/2015/dec/21/beijings-smog-red-alert-enters-third-day-as-toxic-haze-shrouds-city (accessed on 28 May 2016).
4 Nace T. Beijing declares 'red alert' over pollution: haze visible from space. 2015-12-09. Available at: http://www.forbes.com/sites/trevornace/2015/12/09/beijing-declares-red-alert-pollution-haze-visible-space/#75f309ce2c67 (accessed on 28 May 2016).
5 US EPA. Particulate matter (PM) basics. Available at: https://www.epa.gov/pm-pollution/particulate-matter-pm-basics#PM (accessed on 17 October 2016).
6 Loomis D, Grosse Y, Lauby-Secretan B, Ghissassi FE, Bouvard V *et al*. The carcinogenicity of outdoor air pollution. *Lancet Oncol* 2013; **14**: 1262–1263.
7 Harrison D, Maggs R, Booker J. UK equivalence programme for monitoring of particulate matter. Report. No. BV/AQ/AD202209/DH/2396, Bureau Veritas 2006.
8 Model 804 Handheld Particle Counter | Met One Instruments. Available at: http://www.metone.com/products/indoor-particle-monitors/model-804/ (accessed on 10 March 2017).
9 Fluke 985 Indoor Air Quality Particle Counter. Available at: http://en-us.fluke.com/products/hvac-iaq-tools/fluke-985-hvac-iaq.html (accessed on 28 May 2016).
10 TSI Model 3007 hand-held particle counter. Available at: http://www.tsi.com/uploadedFiles/_Site_Root/Products/Literature/Spec_Sheets/3007_1930032.pdf (accessed on 16 November 2016).
11 Center for aerosol science and engineering (CASE). Available at: http://www.aerosols.wustl.edu/Education/default.htm.
12 Orr C, Martin RA. Thermal precipitator for continuous aerosol sampling. *Rev Sci Instrum* 1958; **29**: 129–130.
13 Broßell D, Tröller S, Dziurowitz N, Plitzko S, Linsel G *et al*. A thermal precipitator for the eposition of airborne nanoparticles onto living cells—rationale and development. *J Aerosol Sci* 2013; **63**: 75–86.
14 Liu C, Hsu PC, Lee HW, Ye M, Zheng GY *et al*. Transparent air filter for high-efficiency PM2.5 capture. *Nat Commun* 2015; **6**: 6205.
15 Walton WH, Vincent JH. Aerosol instrumentation in occupational hygiene: an historical perspective. *Aerosol Sci Technol* 1998; **28**: 417–438.
16 Aerosol Instrumentation, Section 3. Available at: http://aerosol.ees.ufl.edu/instrumentation/section03.html (accessed on 28 May 2016).
17 Mudanyali O, Tseng D, Oh C, Isikman SO, Sencan I *et al*. Compact, light-weight and cost-effective microscope based on lensless incoherent holography for telemedicine applications. *Lab Chip* 2010; **10**: 1417–1428.
18 McLeod E, Dincer TU, Veli M, Ertas YN, Nguyen C *et al*. High-throughput and label-free single nanoparticle sizing based on time-resolved on-chip microscopy. *ACS Nano* 2015; **9**: 3265–3273.
19 Gonzalez RC, Woods RE, Eddins SL. *Digital Image Processing Using MATLAB*. Gatesmark Publishing: Knoxville, TN, USA, 2004.
20 Train support vector machine classifier—MATLAB svmtrain. Available at: https://www.mathworks.com/help/stats/svmtrain.html (accessed on 14 November 2016).
21 Grant M, Boyd S. CVX: Matlab software for disciplined convex programming, version 2.10. Available at: http://cvxr.com/cvx/ (accessed on 28 May 2016).
22 Greenbaum A, Luo W, Su TW, Göröcs Z, Xue L *et al*. Imaging without lenses: achievements and remaining challenges of wide-field on-chip microscopy. *Nature Methods* 2012; **9**: 889–895.
23 Bishara W, Su TW, Coskun AF, Ozcan A. Lensfree on-chip microscopy over a wide field-of-view using pixel super-resolution. *Optics Express* 2010; **18**: 11181–11191.
24 Wu Y, Zhang Y, Luo W, Ozcan A. Demosaiced pixel super-resolution for multiplexed holographic color imaging. *Sci Rep* 2016; **6**: 28601.
25 Greenbaum A, Luo W, Khademhosseinieh B, Su T-W, Coskun AF *et al*. Increased space-bandwidth product in pixel super-resolved lensfree on-chip microscopy. *Sci Rep* 2013; **3**: 1717.
26 What is a cleanroom? Cleanroom classifications, class 1, 10, 100, 1 000, 10 000, 100 000, ISO Standard 14644, cleanroom definition. Available at: http://www.cleanairtechnology.com/cleanroom-classifications-class.php (accessed on 28 May 2016).
27 Hollander M, Wolfe DA, Chicken E. *Nonparametric Statistical Methods*. 3rd edition, John Wiley and Sons: New York, 2013.
28 Pascucci C, Ryan K, Cheng K, Pamer M. Sand Fire explodes to over 3 300 acres in Santa Clarita Area; New evacuations ordered in little Tujunga Canyon. KTLA, 2016-07-22. Available at: http://ktla.com/2016/07/22/20-acre-fire-burns-near-sand-canyon-in-santa-clarita/ (accessed on 11 February 2017).
29 SCVNews.com. Sand Fire grows to 3327 Acres; 200–300 evacuations. 2016. Available at: http://scvnews.com/2016/07/22/sand-fire-grows-to-2500-acres-evacuations/ (accessed on 11 February 2017).
30 Quality assurance air monitoring site information, 2014. Available at: https://www.arb.ca.gov/qaweb/site.php?s_arb_code=70074 (accessed on 17 October 2016).
31 Hudda N, Gould T, Hartin K, Larson TV, Fruin SA. Emissions from an international airport increase particle number concentrations 4-fold at 10 km downwind. *Environ Sci Technol* 2014; **48**: 6628–6635.
32 Windfinder.com. Wind and weather statistic Los Angeles Airport. Available at: https://www.windfinder.com/windstatistics/los_angeles_airport (accessed on 14 November 2016).
33 Google Maps. Available at: https://www.google.com/maps/@33.9465247,-118.3382833,1718m/data=!3m1!1e3 (accessed on 6 October 2016).
34 LAX noise management—Noise contour maps. Available at: http://www.lawa.org/welcome_lax.aspx?id=1090 (accessed on 17 October 2016).
35 FlightStats—Global flight tracker, status tracking and airport information. Available at: http://www.flightstats.com/go/Home/home.do (accessed on 17 October 2016).

This work is licensed under a Creative Commons Attribution-NonCommercial-NoDerivs 4.0 International License. The images or other third party material in this article are included in the article's Creative Commons license, unless indicated otherwise in the credit line; if the material is not included under the Creative Commons license, users will need to obtain permission from the license holder to reproduce the material. To view a copy of this license, visit http://creativecommons.org/licenses/by-nc-nd/4.0/

© The Author(s) 2017

Supplementary Information for this article can be found on the *Light: Science & Applications*' website (http://www.nature.com/lsa).